Journal of Vacuum Science and Technology A

RESEARCH ARTICLE | MARCH 06 2020

New approach for an industrial low-temperature roll-to-roll CI(G)Se hybrid sputter coevaporation deposition process

Nikolaus Weinberger; David Stock; Christian Alexander Kaufmann; Tim Kodalle; Marc D. Heinemann; Daniel Huber; Martina Harnisch; Andreas Zimmermann; Georg N. Strauss; Roman Lackner

J. Vac. Sci. Technol. A 38, 033201 (2020)
https://doi.org/10.1116/1.5142830

JVST A
Journal of Vacuum Science & Technology A

ARTICLE

avs.scitation.org/journal/jva

New approach for an industrial low-temperature roll-to-roll CI(G)Se hybrid sputter coevaporation deposition process

Cite as: J. Vac. Sci. Technol. A 38, 033201 (2020); doi: 10.1116/1.5142830
Submitted: 18 December 2019 · Accepted: 12 February 2020 ·
Published Online: 6 March 2020

Nikolaus Weinberger,[1,a)] David Stock,[1] Christian Alexander Kaufmann,[2] Tim Kodalle,[2] Marc D. Heinemann,[2] Daniel Huber,[3] Martina Harnisch,[3] Andreas Zimmermann,[3] Georg N. Strauss,[1] and Roman Lackner[1]

AFFILIATIONS

[1]Department of Structural Engineering and Material Sciences, Unit of Material Technology, University of Innsbruck, Technikerstraße 13, 6020 Innsbruck, Austria
[2]Helmholtz-Zentrum Berlin, Competence Centre Thin-Film- and Nanotechnology for Photovoltaics Berlin, Schwarzschildstraße 3, 12489 Berlin, Germany
[3]Sunplugged GmbH, Mindelheimer Str. 6, 6130 Schwaz, Austria

[a)]**Electronic mail:** nikolaus.weinberger@uibk.ac.at

ABSTRACT

A new industrial approach for the production of $CuInSe_2$ (CISe) absorber layers in a roll-to-roll process is described. This process is used by *Sunplugged GmbH* and combines magnetron sputtering with thermal coevaporation. A CISe-based device with a conversion efficiency of more than 10% has been fabricated from absorbers grown on polyimide at low temperature. The characteristic properties of a copper-poor ([Cu]/[In] = 0.73) CISe layer, deposited by *Sunplugged's* industrial process, are compared to those of a state-of-the-art, more copper-rich ([Cu]/[In] = 0.93) layer, grown in a molecular beam epitaxy system at *Helmholtz-Zentrum Berlin*. The presence of a so called vacancy-compound in low [Cu]/[In] CISe devices exhibiting an increased bandgap energy is visible by external quantum efficiency measurements, Raman scattering, and SCAPS simulations.

I. INTRODUCTION

$CuInSe_2$ (CISe) and related chalcopyrite structures such as $Cu(In,Ga)Se_2$ (CIGSe) are used in thin film photovoltaics (PV). CIGSe technology is progressively understood as a serious competitor to silicon photovoltaics. The current world record in conversion efficiency of 23.35% of CIGSe on rigid glass was achieved by *Solar Frontier* in Japan.[1] It is the highest efficiency of any polycrystalline thin film PV technology. A record efficiency of 20.4% on flexible polyimide substrate was achieved by *EMPA* in Switzerland.[2] Advantages in comparison to silicon wafer-based technology are low material consumption, shorter energy payback time, the monolithic interconnection technique, lower cost, lightweight, and bendability.[3,4] Already in 2000, Schock and Noufi *et al.*[5] pointed out the eminent industrial usability and upcoming challenges of the CIGSe technology.

Flexible substrates, such as steel or polyimide foil, allow a roll-to-roll (R2R) process technology, which guarantees a cost-efficient production and a customizable application of the PV material. The big advantage of polyimide in comparison to steel foil is its lightweight, which is especially interesting, e.g., for space applications or building integrated photovoltaics.

In the last 20 years, several CIGSe deposition technologies have been developed and investigated. Vacuum-based technologies such as three-stage coevaporation,[6,7] sequential procedures,[8] and non-vacuum-based technologies[9] have been developed and investigated. Empirically, two procedures got established on the industrial scale. For example, the three-stage coevaporation process is used on the industrial scale by *Flisom AG* on polyimide foil, by *NICE Solar Energy GmbH* on glass, and by *Global Solar GmbH* on steel foil. The second mainly used process is a sequential process: metallic

layers are selenized after the deposition of a precursor layer, i.e., a metal compound formed by magnetron sputtering. *Solar Frontier* uses a classical sequential process where the precursor stack is selenized for several hours.[10] *Avancis GmbH* uses a technique called rapid thermal processing, which allows for fast selenization.[11]

Sunplugged GmbH (SunP) is a company in Tyrol, Austria, with the aim to produce lightweight and flexible PV modules, customizable in shape and operating voltage. In collaboration with the University of Innsbruck and the University of Milan-Bicocca, *Sunplugged* developed a new approach for the deposition of polycrystalline CIGSe thin films, which promises an energy-efficient industrial production. The CIGSe absorber is formed by an R2R hybrid deposition process, which combines sputtering and thermal coevaporation techniques in one process chamber. It is similar to a classical three-stage process with aspects of a sequential formation process. Due to the relatively high background pressure (10^{-3} mbar) in the deposition chamber, in combination with the volatile behavior of selenium, a selenium atmosphere is present in the whole chamber. To realize the principle of a classical three-stage process,[7] the process chamber is divided into three zones. In order to grow high-quality CISe thin films, In_2Se_3 is deposited in the first zone. In the second zone, $Cu_{2-x}Se$ is added to the layer until a Cu-rich composition of CISe is reached. In the third zone, In_2Se_3 is deposited until a copper-poor composition is reached. The basic concept (lab-scale) was developed by Acciarri *et al.*[12] The R2R deposition machine described in this work was also developed in Italy by Binetti *et al.*, conceptual also shown in Ref. 13. It promises a straightforward upscaling due to the easy scalability of sputter magnetrons and in view of realization of linear flux profiles across the entire width of the substrate foil, as presented in Ref. 14.

In this work, detailed insight in the industrial R2R Hybrid-CIGSe process is given. CISe cells with a conversion efficiency of more than 10% are presented. It should be mentioned that *Sunplugged* uses no gallium in the early development stage. The properties of the CISe absorber grown in a state-of-the-art molecular beam epitaxy (MBE) research chamber with a Cu to In ratio of [Cu]/[In] = 0.93 are compared with those CISe absorbers grown by the industrial Hybrid-CIGSe process with a ratio of [Cu]/[In] = 0.73. The presence and influence of a comparatively thick copper-poor vacancy-compound (VC) at the surface of the CISe absorber grown by *Sunplugged's* method is discussed. This might be interesting especially for industrial approaches, which prefer short process times with respect to copper diffusion kinetics.

II. EXPERIMENT

In this section, the experimental details concerning the device fabrication and the used analytical methods are described, focusing on SunP's CISe process and the absorber deposition process at *Helmholtz-Zentrum Berlin* (HZB).

The back contact of the SunP device consists of a multilayer of 100 nm titanium, 180 nm sodium-doped molybdenum, and 350 nm pristine molybdenum, which is deposited on a 30 cm wide polyimide foil (*Upilex* 25SV5). All back contact layers are deposited by magnetron sputtering in a single R2R in-house-built high vacuum machine ($p_0 < 10^{-5}$ mbar, $p_{process} = 3 \times 10^{-3}$ mbar). For the sodium-doped molybdenum layer, an Mo:Na target with 10 at. % Na from the *Plansee group* is used. The titanium layer functions as a sodium diffusion barrier to avoid Na loss toward the polyimide substrate and as a thermomechanical compensation between the different thermal expansion coefficients of Pl and Mo [$\alpha_{polyimide} = 12\,\mu m\,K^{-1}$ commercially available; $\alpha_{Ti} = 8.6\,\mu m\,K^{-1}$; $\alpha_{Mo} = 4.8\,\mu m\,K^{-1}$ (values are valid at 20 °C)]. For the HZB device, an 800 nm molybdenum layer deposited on soda lime glass by magnetron sputtering is used as a back contact.

A. CISe absorber growth

Absorbers for *Sunplugged* devices are produced with the Hybrid-CISe process (SunP process). The deposition chamber is divided into three zones, to realize the concept of a three-stage coevaporation process in the R2R configuration. Every zone consists of a sector for magnetron sputtering, a cylindrical transfer device, and an evaporation region. Each cylindrical transfer device consists of 60 graphite bars, arranged in a cylindrical geometry, as shown in Fig. 1(b). A picture of the smaller version of the transfer device is shown in Ref. 14. Initially, the metals are deposited onto the cylindrical transfer device by magnetron sputtering. This requires an argon pressure of $\sim 3 \times 10^{-3}$ mbar to be present in the deposition chamber. After the metal deposition, the graphite bar, part of the cylindrical transfer device, rotates to point in the direction of the substrate. There, the metal is re-evaporated from the bars and deposited onto the substrate in an Se atmosphere. By stepwise rotation and application of a current to the individual graphite bar, the evaporating metals create a periodical flux profile. The power applied to the respective magnetron controls the amount of the individual metals, while the evaporation lasts until the sputtered material is completely evaporated from the respective bar. The selenium vapor is introduced via thermal evaporation using infusion cells. The temperature of the molten selenium controls the

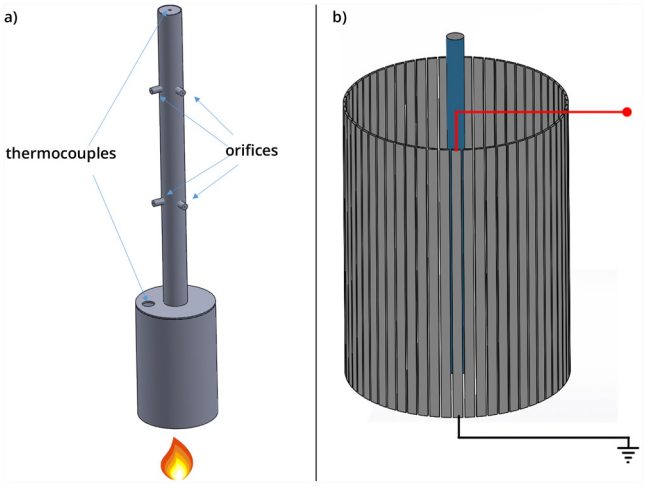

FIG. 1. (a) 3D model of the selenium source; temperature-controlled infusion cell made of graphite. Separately heated melt and vapor region. (b) 3D model of the cylindrical transfer device.

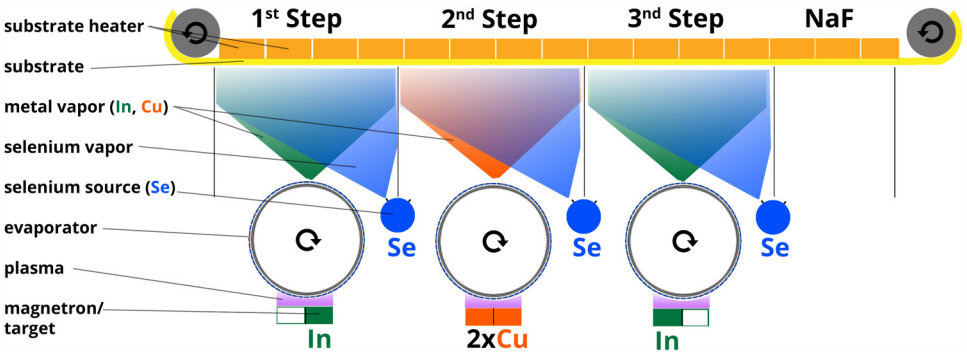

FIG. 2. Top view of Sunplugged's CI(G)Se deposition process. Metal components are sputtered on graphite bars and subsequently evaporated and deposited on the polyimide substrate. Selenium is introduced by temperature-controlled infusion cells.

amount of selenium. Schematic of the selenium source are shown in Fig. 1(a). Further details are described in Sec. IV A.

In the first and third zone, an indium sputter target is used; in the second zone, two copper targets are located. To adjust the ratio between selenium and metal, all three zones are equipped with a separate selenium source. Fourteen separately controlled heaters included in the substrate holder provide a defined substrate temperature profile. The individual zones are geometrically separated by metal shielding. Figure 2 depicts a top view schematic of the described CISe process at *Sunplugged*.

The reference CISe sample is produced in a state-of-the-art MBE deposition chamber located at HZB. A classical three-stage coevaporation process was used, with further details described in Ref. 15. The substrate temperature T_{sub} for the three steps/zones was set to $T_{sub1} = 300\,°C$, $T_{sub2} = 460\,°C$, and $T_{sub3} = 460\,°C$ for both CISe processes. All top layer deposition and cell fabrication for both samples were done at HZB.

On *Sunplugged's* CISe deposition machine, two processes are described in this work:

1. Deposition of copper with velocity of the substrate $v_{sub} = 0$ mm/s for investigation of the metal flux distribution.
2. To fabricate a device, a CISe layer with a final [Cu]/[In] = 0.73 was grown. Copper-rich growth was realized by reaching a nominal copper to indium ratio of $[Cu]/[In]_{2step} = 1.16$ after the second zone. The metal to selenium ratio (Se/M) varies continuously. Calculations in Sec. IV A result in a range of $1.1 < [Se]/[M] < 2.5$. The substrate velocity was set to $v_{sub} = 0.5$ mm/s. Total deposition duration for the formed CISe layer was 3240 s.

The CISe reference sample at HZB was also made, ensuring Cu-rich growth, reaching $[Cu]/[In]_{2step} = 1.8$ and a final [Cu]/[In] ratio of 0.9. The selenium to metal ratio was set to $[Se]/[M] > 3$ throughout the whole process.

B. Top layers and contacts

To finish the devices, a CdS buffer layer ($d = 40$–60 nm) is grown by chemical bath deposition (CBD). An intermediate i-ZnO ($d = 40$ nm) and the front contact Al:ZnO ($d = 130$ nm) are both deposited via magnetron sputtering. After depositing Al/Ni/Al contact fingers, the solar cells are defined by mechanical scribing. The cell size for both types of absorbers is 1 cm². These tasks were performed at HZB standard CIGSe cell fabrication line, further described in Ref. 15.

C. Analytical methods

Tilted (60°) and cross-sectional images of the CISe layer were captured with a scanning electron microscope (SEM) (*JEOL 7610F*). The SEM pictures were made in the high-resolution mode (pressure $p \approx 4 \times 10^{-6}$ mbar). The samples were coated with a thin (5 nm) gold layer (*Agar Sputter Coater*) to prevent charging. The accelerating voltage was set to 15 keV, and the working distance was between 7 and 9 mm. For the tilted and cross-sectional pictures, a secondary electron in-lens and a backscattered electron detector were used. The elemental composition was measured by wavelength dispersive x-ray fluorescence spectroscopy (XRF) using a *Rigaku Primus II+*. K-shell intensity of Cu, In, Se, and Mo was used to evaluate the content by quantitative fundamental parameter analysis. The excitation energy was set to 50 keV. The measurements were performed without CdS and ZnO/AZO layers. Raman spectra were done with a system based on *S&I components* equipped with a laser emitting light at a wavelength of 532 nm. For Raman spectra of the backside of the CISe layer, a lift-off with double-sided polyimide tape was done. Current-voltage (IV) measurements were performed under AM1.5 illumination at room temperature under a *Pasan* sun simulator. For external quantum efficiency (EQE) measurements, an in-house-built system at HZB was used.

III. RESULTS AND DISCUSSION

A. Hybrid-CIGSe process investigations

Similar to the flux diagram in Ref. 16 for sequential three-stage coevaporation processes described in Ref. 7, the aim of this part in the present work is to calculate a flux diagram. It schematically describes the R2R CISe process in *Sunplugged's* hybrid deposition chamber. The material flux, reaching the substrate is dependent on the position with reference to the source of the respective material. In order to determine a flux diagram, the evaporation characteristics of the graphite bars are determined. Hence, the substrate velocity v_{sub} was set to zero ($v_{sub} = 0$ mm/s). The spatial rate distribution of the evaporation drum in the second zone was investigated by measuring the position dependent layer thickness. Using a coordinate system with the x-direction parallel

to the substrate velocity and the y-direction in the substrate plane perpendicular to the substrate velocity ($y = 0$ in the middle of the substrate), the thickness distribution of the resulting layer in the Cu zone including a curve fit is shown in Fig. 3. Due to selenium contamination in the chamber, the resulting layer is not pure copper, but copper-selenide (Cu_2Se). The following function was applied for fitting:

$$d(x) = d_{\max} \cdot \cos^2\left(\pi \frac{x - x_{\max}}{w}\right), \tag{1}$$

with the position x, $x_{\max}$ is the position of the max thickness, $d_{\max}$ is the max thickness, and w refers to the width of the distribution in the x-direction. It has to be mentioned that the amplitude or maximum layer thickness $d_{\max}$ in Eq. (1) varies with the amount of Se during CISe process conditions; nevertheless, the characteristics of the distribution are described very well. This distribution function was used to plot a flux diagram for the actual growth process of the CISe to fabricate a complete solar device.

To determine the metal flux I for the flux diagram, compositional proportions of weight w_{metal} and thickness values d^{XRF} (measured by XRF) were used to estimate the particle density n_{metal} of the individual metals of the finished CISe layer. Considering the relation between substrate velocity v_{sub} and deposition duration t ($v_{\text{sub}} = \Delta x_{\text{zone}}/t$), the resulting metal flux I can be calculated. To receive the maximum metal flux $I^{\max}$, n_{metal} is divided by the integrated normalized distribution [Eq. (1)]. Finally, Eq. (1) was used to get the position-depending flux distribution $I(x)$. The equations for the described physical quantities are Eqs. (2)–(4), with Avogadro constant N_A,

$$n_{\text{Cu}}\left[\frac{\text{N}}{\text{cm}^2}\right] = w_{\text{Cu}}^{\text{XRF}} \cdot d_{\text{CISe}}^{\text{XRF}} \cdot \rho_{\text{CISe}} \frac{N_A}{M_{\text{Cu}}}, \tag{2}$$

$$I_{\text{Cu}}^{\max}\left[\frac{\text{N}}{\text{cm}^2\text{s}}\right] = n_{\text{Cu}} \frac{1}{\int_{x_1}^{x_2} \cos^2\left(\pi \frac{x - x_{\max}}{w}\right) dx} \cdot \frac{v_{\text{sub}}}{\Delta x_{\text{Cu\_zone}}}, \tag{3}$$

$$I_{\text{Cu}}(x)\left[\frac{\text{N}}{\text{cm}^2\text{s}}\right] = I_{\text{Cu}}^{\max} \cos^2\left(\pi \frac{x - x_{\max}}{w}\right). \tag{4}$$

The total selenium flux per source Γ_{Se} is calculated by the Knudsen effusion equation[17] and the flux distribution $I_{\text{Se}}(\vartheta)$ by cosine law of emission. The corresponding equations are Eqs. (5) and (6). Figure 4 shows geometrical details; for further details of the calculation, see Ref. 17.

$$\Gamma_{\text{Se}} = 3.51 \times 10^{22} \frac{pA_e}{\sqrt{MT}}, \tag{5}$$

$$I_{\text{Se}}(\vartheta) = \frac{\Gamma_{\text{Se}}}{\pi r^2} \frac{r_A^2}{r_B^2} \cos\vartheta \cos(\vartheta + \phi). \tag{6}$$

With the total selenium flux Γ_{Se}, the vapor pressure in the selenium source p, the area of the nozzle A_e, the temperature of the selenium melt T, the atomic mass of selenium M, and the geometrical quantities r, r_A, r_B, ϕ, and ϑ are described in Fig. 4.

By assuming that metal rates are linearly proportional to the sputtering power of the magnetrons and applying the above equations in all three zones, one can obtain the flux diagram [see Fig. 5(a)]. Moreover, the indium flux in zone 1 and zone 3 is calculated by applying the ratio of the sputter power of the two zones to the total indium flux. The position x of the sample in the CISe machine is shown on the bottom x-axis. In Fig. 5(b), the evolution of the [Cu]/[In] ratio during the layer growth is indicated.

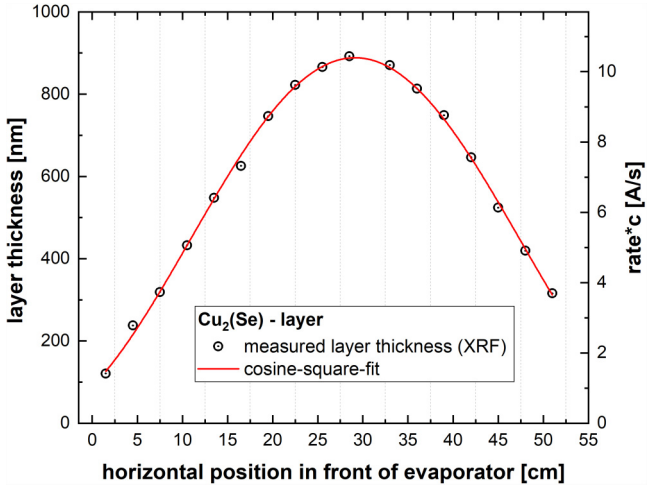

FIG. 3. Layer thickness in front of the evaporator measured by XRF proportional to metal rate; solid line: cosine-square fit.

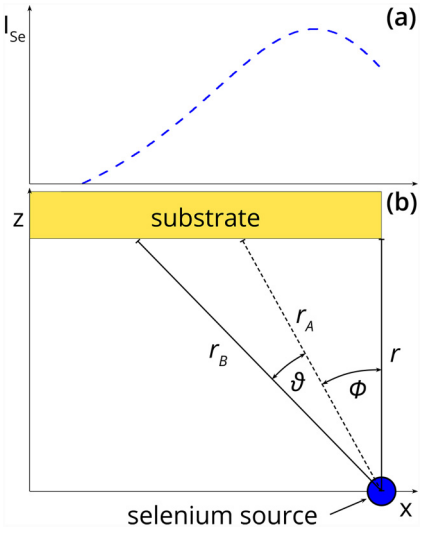

FIG. 4. (a) Resulting selenium flux distribution; (b) schematic of geometrical details for the calculation of the selenium flux distribution.

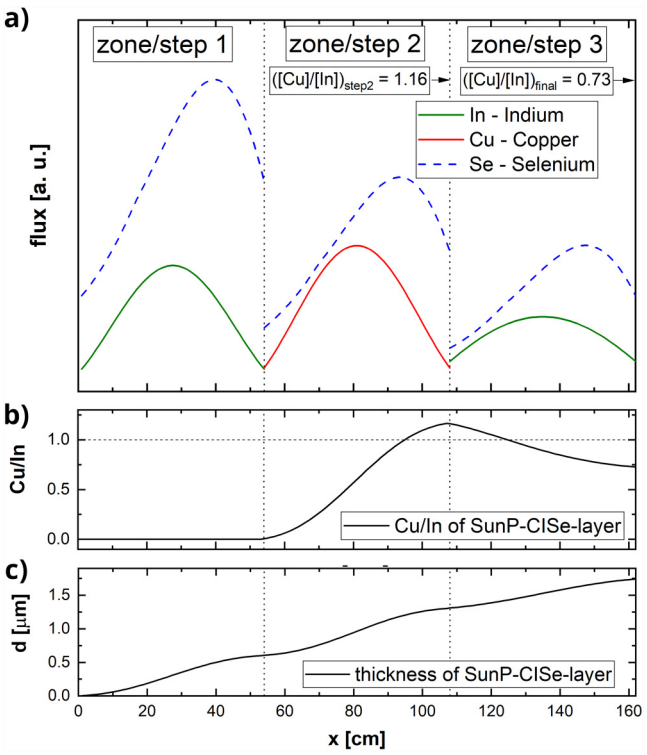

FIG. 5. (a) Flux diagram of the R2R SunP process. On the bottom *x*-axis, the position of the sample in the CISe deposition machine is plotted. (b) The evolution of the [Cu]/[In] ratio is plotted. (c) The resulting layer thickness is shown; *x* can be substituted by *t* using the relation $t = x/v_{sub}$.

A copper-rich ([Cu]/[In] > 1) composition is reached after the second zone. The nonlinear increasing layer thickness *d*, due to the flux distributions, is shown in Fig. 5(c). Besides the higher process pressure (10^{-3} mbar), the SunP process exhibits another major difference to a classical three-stage process. The evaporation technique of *Sunplugged* implicates pulsed metal fluxes, which is schematically shown (not actual frequency and pulse ratio) in Fig. 6. This has the consequence that the selenium to metal ratio is not constant. It has to be mentioned that re-evaporation of metals, selenium, or mixed compounds were neglected for the calculated flux diagram.

IV. CHARACTERIZATION AND DISCUSSION

In this part of the presented work, the CISe absorber manufactured with the Hybrid-SunP process as well as a completed device are compared to a cell from a laboratory scaled, conventional sequential three-stage coevaporation process at HZB. The industry often uses lower [Cu]/[In] ratios than research institutions in order to prevent shunts due to malicious lateral inhomogeneity. Due to the geometry of coevaporation tools used elsewhere, lateral inhomogeneities of up to 10%–15% across large samples are observed. This and possible "spitting" of evaporation

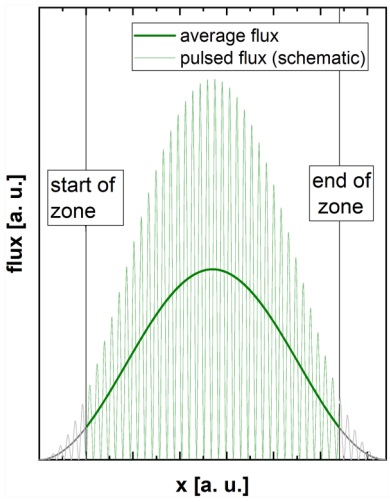

FIG. 6. Schematic plot of the pulsed metal flux in the first zone. Frequency is the same for zones 2 and 3. The parts before and after the actual zone of the curve (thin and thick) demonstrate the metals deposited on the shielding between the zones.

sources forces manufacturers to use overall lower [Cu]/[In] ratios than research institutions. A thin VC layer of a few nanometers is generally desirable, as it passivates the interface between the absorber and the buffer layer.

A. Material characterization

The copper to indium ratio and the thickness *d* were determined by XRF. The resulting values are summarized in Table I. The chosen [Cu]/[In] ratio reflects the difference between industrial and lab-scale processes.

Figure 7 shows cross-sectional and tilted surface SEM images of the CISe layer. In Fig. 7(b), a density/phase difference (a slightly brighter section) in the surface/top region of the CISe layer is revealed by detecting the backscattered electrons. With respect to the total [Cu]/[In] ratio [see also Fig. 5(b)], it is expected to be a Cu-poor phase. Raman measurements from the front and back sides (as described in Sec. III C) confirmed the existence of a Cu-poor VC, such as $CuIn_{1,5}Se_2$, $CuIn_2Se_{3,5}$, $CuIn_3Se_5$, or $CuIn_5Se_8$ at the surface (see Fig. 8). According to Refs. 16 and 18, the vibrational modes of the different VC occur in the wavenumber region between 151 and 156 cm^{-1}.

TABLE I. Copper to indium ratio and layer thickness of SunP and HZB samples measured with XRF.

Sample	[Cu]/[In] ratio	Thickness *d* (µm)
SunP CISe	0.73	1.74
HZB CISe	0.93	2.83

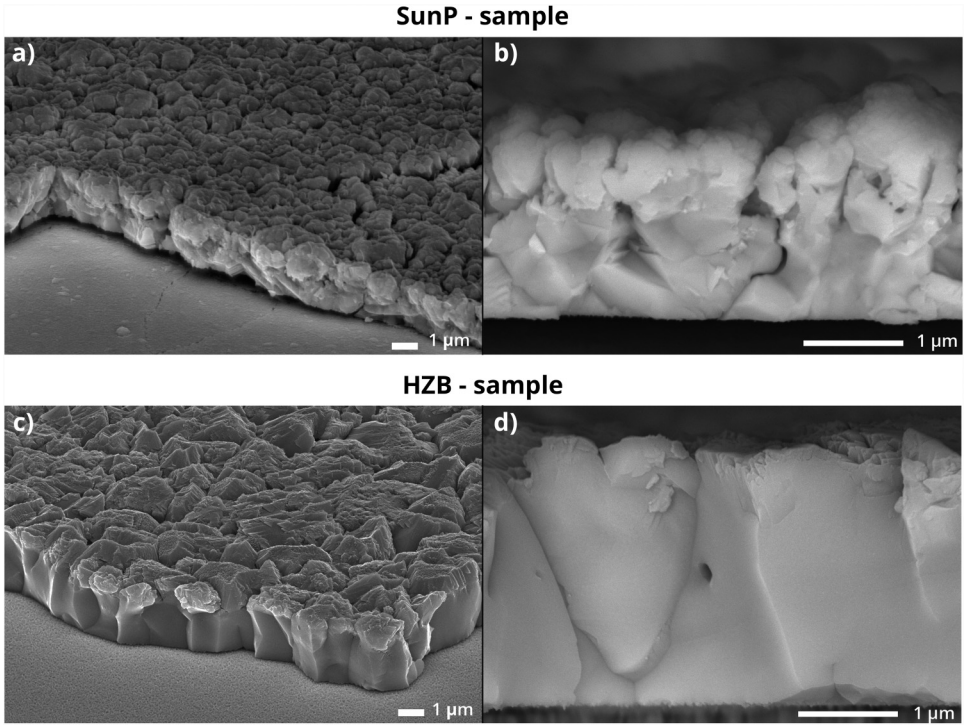

FIG. 7. SEM images of the CISe layers. (a) and (c): tilt = 60°, high-resolution in-lens ET detector; (b) and (d): tilt = 90°, BE detector. The cross section of the SunP sample [(a) and (b)] ([Cu]/[In] = 0.73) shows, in contrast to the HZB sample [(c) and (d)] ([Cu]/[In] = 0.93), a light gray region on the top, which refers to the VC due to a higher amount of indium.

B. Device characterization

The resulting IV curves in the dark and under illumination of the best devices are presented in Fig. 9. The HZB device shows a slightly lower open circuit voltage (V_{OC}) than the SunP device, while the fill factor (*FF*) is higher. The short circuit current density (j_{sc}) is comparable. ΔV_{OC} was calculated by subtracting V_{OC} from bandgap energy E_g determined out of the EQE. The device data are summarized in Table II. It should be mentioned that a maximum efficiency of 14.5% for CISe cells (without Ga) has been reached with optimized devices (not at low T_{sub}).[19]

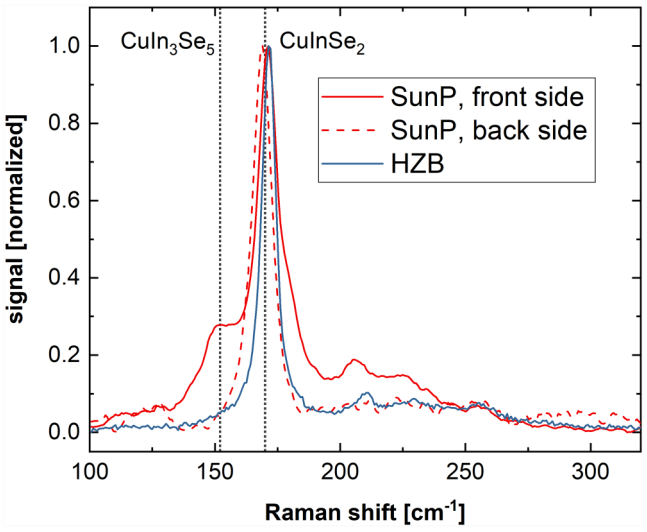

FIG. 8. Raman spectra for distinction of VC: dotted vertical lines refer to $CuInSe_2$ and to $CuIn_3Se_5$ phases.

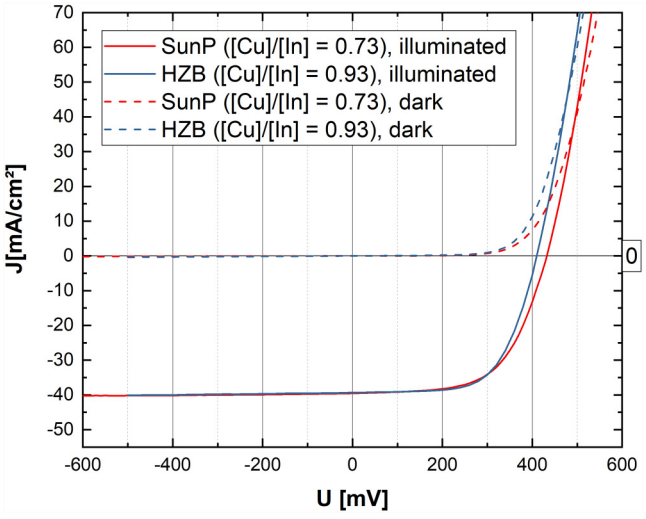

FIG. 9. IV curves of investigated devices.

TABLE II. Device data of the HZB and SunP devices are summarized.

Device	V_{oc} (mV)	j_{sc} (mA/cm^2)	FF (%)	η (%)	ΔV_{OC} (mV)
SunP cell	432	39.5	60.1	10.3	568
HZB cell	410	39.3	63.7	10.3	590

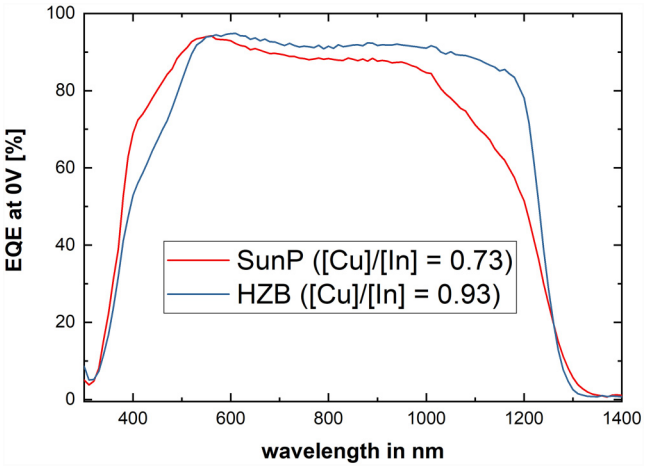

FIG. 10. EQEs of CISe thin film devices are shown. The SunP device shows a slightly improved current collection in the region around 400 nm, while a decreased current collection in the region of > 1000 nm.

With the lab-scale Hybrid-CIGSe process at the University of Milan-Bicocca, an efficiency of 10.1% for a device with gallium on polyimide deposited at low temperature was reported.[13] The comparison of the SunP device data with the data of the HZB device, regarding the low substrate temperature, conclude that the SunP process is able to form absorbers with similar performance.

The EQEs of both samples are shown in Fig. 10. As presented in Ref. 20, the bandgap of the VC is about 1.2 eV. The reduced current collection in the region of 1000–1300 nm is attributed to a pronounced presence of a VC layer at the surface of the thin film, as was already indicated in Fig. 7(a). This effect is also reported in Ref. 16. The increased current collection in the region of 380–550 nm, which is observed for the SunP device, is attributed to a difference in the CdS buffer layer growth. For example, a thinner CdS layer would decrease the loss by parasitic absorption. The buffer layers of both devices were prepared following the same CBD procedure indicating that the growth of the CdS is not directly altered by the process conditions but indirectly by the different growth substrates (i.e., SunP and HZB surfaces). Both, morphology and chemical composition could affect the growth of the CdS layer. Cd also could intercalate in the copper-poor VC and occupy copper vacancies, which could lead to a thinner CdS layer. This might also result in a different bandgap of the CdS layer as described in Ref. 21.

For a better understanding of the reduced EQE at longer wavelength, SCAPS simulations[22] have been performed (input values in the Appendix) with a variation of the VC layer thickness (d_{VC}) and the free charge carrier density (N_A). As seen in Fig. 11(a), the EQE at longer wavelength is strongly reduced for VC layer thicknesses above 250 nm. The simulation result for 375 nm VC layer thickness is in good accordance with the

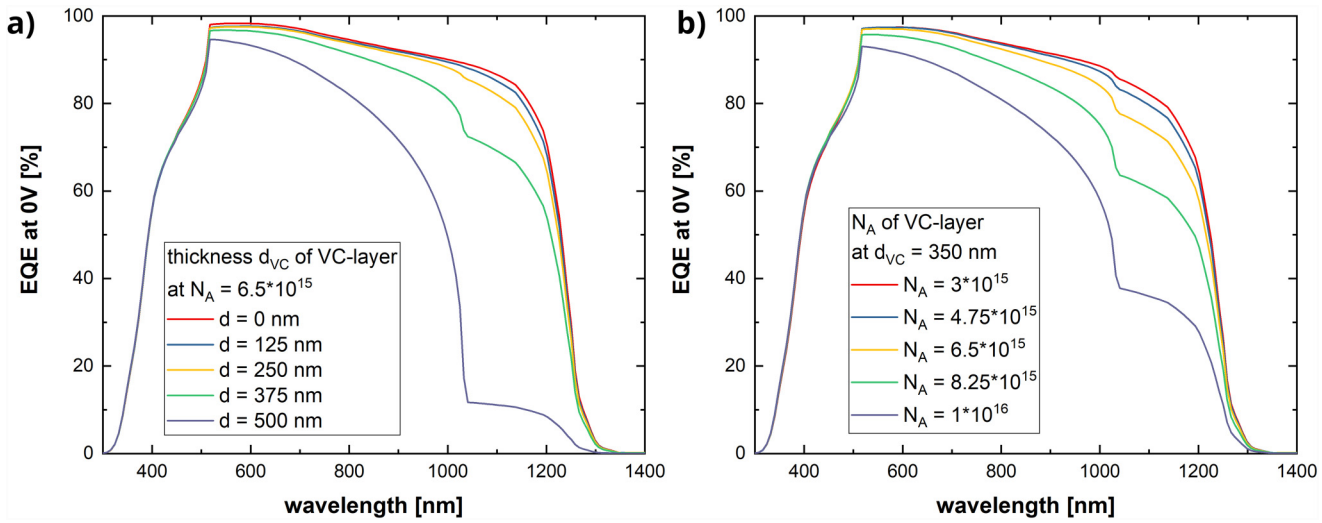

FIG. 11. Simulations with SCAPS 3.307 were performed to describe the EQE behavior of the VC layer on top of the CISe layer. Due to absorption of photons with a wavelength higher than 1033 nm (E_g = 1.2 eV), the current collection decreases with increasing VC thickness, shown in (a). A similar effect results by increasing the charge carrier density N_A of the VC layer, shown in (b).

experimental EQE result and with VC layer thickness observed in the SEM image in Fig. 7(b). This could be due to a reduced total light absorption, since the VC does not absorb photons with wavelengths longer than 1033 nm ($E_g = 1.2$ eV). The EQE clearly shows an increased recombination current with increased VC thickness. Due to that fact, that the low energy photon absorption takes place only in the CISe layer beneath the VC layer and electrons generated by these photons have to diffuse a longer distance (through the VC) to reach the front contact, which increases recombination losses along the way. This effect has to be dependent on the doping density of the VC layer, as this influences the collection efficiency by altering the width of the space charge region. A variation of the doping density within the simulation model is shown in Fig. 11(b). Note that the charge carrier density of the CISe layer was set to $N_A = 3 \times 10^{15}$ cm^{-3}. The simulation results suggest that the free charge carrier density of the VC layer is increased compared to the CISe layer, which is in accordance with the general assumption that the occurrence of increased copper vacancies in the VC layer result in a higher N_A.[23]

V. CONCLUSION AND OUTLOOK

The concept of a new approach for an industrial R2R CISe production process technology has been described. A flux diagram was calculated in order to depict the characteristics of the R2R process. Devices with low temperature grown CISe on polyimide substrates were produced in *Sunplugged's* semi-industrial production unit, showing promising cell performance with an efficiency of $\eta > 10\%$ and a $\Delta V_{OC} = 568$ mV. A low [Cu]/[In] ratio of 0.73 was chosen to prevent shunts. The downside of a low [Cu]/[In] ratio is the formation of a distinct VC compound at the surface. A thin VC layer of a few nanometers usually is desirable, as it passivates the interface between absorber and buffer and, therefore, increases cell performance. If the VC layer becomes thicker, parasitic absorption in the VC decreases the current collection, especially in the near infrared region, which is evident in the EQE results presented in this work. Then again, the different nature of surface (composition and morphology) seems to affect the CdS growth, which resulted in an enhanced current collection above the bandgap energy of CdS, when compared to a device with a lab-produced absorber with a [Cu]/[In] ratio of 0.93. *Sunplugged* currently integrates gallium in their process and a higher process temperature can be used due to the application of steel foil as a substrate. The implementation of a double graded gallium profile in Sunplugged's CIGSe absorber should lead to economical exploitable efficiencies. Besides, alkali post deposition treatments with NaF, KF, or RbF could be applied to reach higher efficiencies.

ACKNOWLEDGMENTS

The authors thank J. Lauche, I. Dorbandt, T. Münchenberg, and K. Mack. The work was done in the framework of the FFG projects Route 16.6 (No. 6184695) and NoFRONTIERS (No. 21588233). The authors also acknowledge the Austrian funding agency FFG and the Austrian Klima- und Energiefonds for the financial support.

APPENDIX

Table III shows the input-parameters for the SCAPS simulation. The absorption models used for the individual layers are mentioned.

TABLE III. Values of the input-parameters for the SCAPS simulation are summarized. Additionally, the chosen absorption models, either measured or calculated, for the different layers are defined.

Settings in SCAPS simulations	Unit	BC	CISe	VC	CdS	ZnO
Thickness	μm	—	1.74	Variation	0.06	0.15
Bandgap	eV	—	1	1.2	2.4	3.3
Electron affinity	eV	—	4.6	4.6	4.3	4.45
Dielectric permittivity	Relative	—	13.6	13.6	10	9
CB effective density of states	1/cm^3	—	2.20×10^{18}	2.20×10^{18}	2.20×10^{18}	2.20×10^{18}
VB effective density of states	1/cm^3	—	1.80×10^{19}	1.80×10^{19}	1.80×10^{19}	1.80×10^{19}
Electron thermal velocity	cm/s	—	1.0×10^{7}	1.0×10^{7}	1.0×10^{7}	1.0×10^{7}
Hole thermal velocity	cm/s	—	1.0×10^{7}	1.0×10^{7}	1.0×10^{7}	1.0×10^{7}
Electron mobility	cm^2/V s	—	100	100	100	40
Hole mobility	cm^2/V s	—	25	25	25	25
Shallow uniform donor density N_D	1/cm^3	—	10	10	1.0×10^{16}	1.0×10^{20}
Shallow uniform acceptor density N_A	1/cm^3	—	3.0×10^{15}	Variation	1	1.0×10^{15}
Absorption model CISe	—	—	Measured absorption of CISe			
Absorption model VC	—	—	—	Square root adsorption model		
Absorption model CdS	—	—	—	—	Square root adsorption model	
Absorption model ZnO	—	—	—	—	—	Measured absorption of ZnO layer

REFERENCES

[1]M. Nakamura, K. Yamaguchi, Y. Kimoto, Y. Yasaki, T. Kato, and H. Sugimoto, IEEE J. Photovoltaics **9**, 1863 (2019).
[2]A. Chirilă *et al.*, Nat. Mater. **12**, 1107 (2013).
[3]M. Powalla, S. Paetel, D. Hariskos, R. Wuerz, F. Kessler, P. Lechner, W. Wischmann, and T. M. Friedlmeier, Engineering **3**, 445 (2017).
[4]J. Ramanujam and U. P. Singh, Energy Environ. Sci. **10**, 1306 (2017).
[5]H.-W. Schock and R. Noufi, Prog. Photovolt. **8**, 151 (2000).
[6]K. Ramanathan *et al.*, Prog. Photovolt. **11**, 225 (2003).
[7]A. M. Gabor, J. R. Tuttle, D. S. Albin, M. A. Contreras, R. Noufi, and A. M. Hermann, Appl. Phys. Lett. **65**, 198 (1994).
[8]T. Kato, Jpn. J. Appl. Phys. **56**, 04CA02 (2017).
[9]M. Kaelin, D. Rudmann, and A. N. Tiwari, Sol. Energy **77**, 749 (2004).
[10]IEEE, *Conference Record of the Twenty Fifth IEEE Photovoltaic Specialists Conference, 1996*, Washington, DC, May 13–17, 1996 (IEEE, New York, 1996).
[11]J. Palm, V. Probst, and F. H. Karg, Sol. Energy **77**, 757 (2004).
[12]M. Acciarri, A. Le Donne, M. Morgano, L. Caccamo, L. Miglio, S. Marchionna, R. Moneta, M. Meschia, and S. Binetti, Energy Proc. **10**, 138 (2011).
[13]S. Binetti, P. Garattini, R. Mereu, A. Le Donne, S. Marchionna, A. Gasparotto, M. Meschia, I. Pinus, and M. Acciarri, Semicond. Sci. Technol. **30**, 105006 (2015).
[14]M. Acciarri, A. Le Donne, S. Marchionna, M. Meschia, J. Parravicini, A. Gasparotto, and S. Binetti, Sol. Energy **175**, 16 (2018).
[15]M. D. Heinemann, R. Mainz, F. Österle, H. Rodriguez-Alvarez, D. Greiner, C. A. Kaufmann, and T. Unold, Sci. Rep. **7**, 45463 (2017).
[16]R. Caballero *et al.*, Acta Mater. **58**, 3468 (2010).
[17]U. Gonser, R. M. Osgood, M. B. Panish, H. Sakaki, H. K. V. Lotsch, M. A. Herman, and H. Sitter, *Molecular Beam Epitaxy* (Springer, Berlin, 1996).
[18]C.-M. Xu, X.-L. Xu, J. Xu, X.-J. Yang, J. Zuo, N. Kong, W.-H. Huang, and H.-T. Liu, Semicond. Sci. Technol. **19**, 1201 (2004).
[19]J. A. M. AbuShama, S. Johnston, T. Moriarty, G. Teeter, K. Ramanathan, and R. Noufi, Prog. Photovolt. **12**, 39 (2004).
[20]D. Schmid, M. Ruckh, F. Grunwald, and H. W. Schock, J. Appl. Phys. **73**, 2902 (1993).
[21]A. Cortes, Sol. Energy Mater. Sol. Cells **82**, 21 (2004).
[22]M. Burgelman, P. Nollet, and S. Degrave, Thin Solid Films **361–362**, 527 (2000).
[23]S. B. Zhang, S.-H. Wei, A. Zunger, and H. Katayama-Yoshida, Phys. Rev. B **57**, 9642 (1998).